



A Lattice Boltzmann Method for Horizontal Axis Wind Turbine Simulation

Stephen L. Wood¹, Ralf Deiterding²

¹ The Bredesen Center, University of Tennessee, Knoxville, TN 37996, USA

² German Aerospace Center (DLR), Institute for Aerodynamics and Flow Technology, Bunsenstr.10, Göttingen, Germany
email: swood@utk.edu, ralf.deiterding@dlr.de

ABSTRACT: Operating horizontal axis wind turbines (HAWT) generate large-scale wake structures that can have considerable impact on downwind turbines. A HAWT exposed to vortices from upwind turbines generally produces reduced power and experiences increased structural vibrations that cause disproportionately accelerated material fatigue. Numerical simulation of the turbulent flow field is a viable approach to improve the understanding of vortex-turbine interactions and to optimize the control and layout of a wind farm. HAWTs are commonly represented with actuator disc or line models in array simulations due to the difficulties of solving the incompressible or weakly-compressible Navier-Stokes equations on moving three-dimensional meshes effectively, cf. [21]. As an alternative to the presently employed methods, we have developed a novel parallel adaptive lattice Boltzmann method for large eddy simulation of turbulent weakly compressible flows with embedded moving structures. Power and thrust coefficients are predicted within 5% of manufacturer's specifications [28]. Wake velocity and pressure deficits along with their fluctuations are scrutinized in the near wake region of a Vestas V27 turbine revealing the three dimensional interactions induced by tower and ground vortex sheets. Simulations of the U.S. Department of Energy's Scaled Wind Farm Technology facility show the influence of an upwind turbine's tower on its wake extends to the down wind turbine. These results confirm that the approach is capable of simulating realistic operation of Vestas 27 turbines including tower and ground interaction accurately for moderate computational cost.

KEY WORDS: Lattice Boltzmann method; Large Eddy Simulation; wind turbines; wake field prediction.

1 INTRODUCTION

Operating horizontal axis wind turbines (HAWT) generate large-scale wake structures that can have considerable impact on downwind turbines. A HAWT exposed to vortices from upwind turbines generally produces reduced power and experiences increased structural vibrations that cause disproportionately accelerated material fatigue. Numerical simulation of the turbulent flow field is a viable approach to improve the understanding of vortex-turbine interactions and to optimize the control and layout of a wind farm. HAWTs are commonly represented with actuator disc or line models in array simulations due to the difficulties of solving the incompressible or weakly-compressible Navier-Stokes equations on moving three-dimensional meshes effectively, cf. [21]. Actuator disc models can be useful in performing a comprehensive simulation of a wind farm wake but they are intrinsically affected by errors in the near wake region; this is due not only to the lack of geometric representation of the rotor, and tower but also to the inability of the model to reproduce the detailed flow physics of the problem [5][19].

More recent simulation efforts represent HAWTs as line actuators and employ blade element theory (BEMT) to determine the flow and forces on blade sections based on 2D steady state airfoil data [11]. Unfortunately, blade element theory contains fundamentally invalid assumptions [29][17] that are overcome in practice by empirical adjustments. There is a widespread desire in the wind industry that a more theoretically correct approach should supplant BEMT in the long term [29]. Full 3D simulations of turbines including support structures and topography have recently been conducted with commercial Navier-Stokes solvers [15] and academic solvers [3] using overset grids to capture turbine motion. Experimental investigations and simulations considering realistic turbine geometry reveal that 3D turbulent wake structures with rotational motion induced by the turbine blades form an inner region where blade and tower vortices interact and an outer region where strong tip vortices dominate the flow [15][16][29][30].

As an alternative to the presently employed methods, we have developed a novel parallel adaptive lattice Boltzmann method for large eddy simulation of turbulent weakly compressible flows with embedded moving structures. This approach is capable of simulating complex near wake interactions and is also scalable to turbine arrays. In this paper we present an overview of the computational approach in Section 1, verification of the method for a canonical rigid body fluid structure interaction experiment in Section 2, a detailed near wake analysis of a Vestas V27 turbine in Section 3, results from simulations of the U.S. Department of Energy's Scaled Wind Farm Technology (SWIFT) facility in Section 4, conclusions in Section 5, and an outlook toward aeroelastic simulations in Section 6.

1 COMPUTATIONAL APPROACH

1.1 Adaptive lattice Boltzmann Method

Macroscopic methods for computational fluid dynamics (CFD) solve the Navier-Stokes (NS) equations to obtain the variables of interest such as velocity \mathbf{u} and pressure p . CFD solvers for the incompressible NS equations need to solve an elliptic equation to obtain the pressure field. Such methods are normally time-implicit and require global data communications while the LBM is time-explicit, only requiring nearest-neighbor communication, and pressures are obtained from an equation of state [27]. The lattice Boltzmann method is based on computing approximations of the Boltzmann equation with a simplified collision operator

$$\partial_t f + \mathbf{u} \cdot \nabla f = \omega (f^{eq} - f) \quad (1)$$

on a rectangular grid of characteristic domain length L with isotropic mesh spacing Δx under the assumption of a small Knudsen number $\text{Kn} = l_f/L \ll 1$, where the mean free path length l_f is replaced with Δx . A crucial idea of the LBM is to approximate Eq. (1) in a specially chosen discrete phase space, in which a partial density distribution function $f_\alpha(\mathbf{x}, t)$ is associated to every discrete lattice velocity \mathbf{e}_α . The total density distribution is given as $\rho(\mathbf{x}, t) = \sum_\alpha f_\alpha(\mathbf{x}, t)$ and the macroscopic moments as $\rho(\mathbf{x}, t) \mathbf{u}_i(\mathbf{x}, t) = \sum_\alpha \mathbf{e}_{\alpha i} f_\alpha(\mathbf{x}, t)$. A splitting approach is then adopted that first solves the homogeneous transport equation with the time-explicit update step

$$T: \tilde{f}_\alpha(\mathbf{x} + \mathbf{e}_\alpha \Delta t, t + \Delta t) = f_\alpha(\mathbf{x}, t). \quad (2)$$

Here, we apply the D3Q19 model for which the lattice velocities are shown in Figure 1 and are defined as

$$\mathbf{e}_\alpha = \begin{cases} 0, & \alpha = 0, \\ (\pm 1, 0, 0)c, (0, \pm 1, 0)c, (0, 0, \pm 1)c, & \alpha = 1, \dots, 6, \\ (\pm 1, \pm 1, 0)c, (\pm 1, 0, \pm 1)c, (0, \pm 1, \pm 1)c & \alpha = 7, \dots, 18, \end{cases} \quad (3)$$

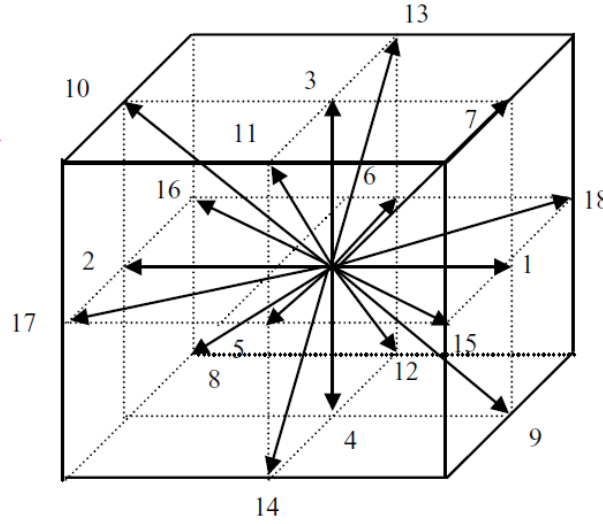


Figure 1. The velocities \mathbf{e}_α of the D3Q19 lattice.

with $c = \Delta x/\Delta t$, which is related to the physical speed of sound by $c_s = c/\sqrt{3}$. The right-hand of Eq. (1) is integrated subsequently by the Bhatnagar-Gross-Krook collision operator [9]

$$C: f_\alpha(\cdot, t) = \tilde{f}_\alpha(\cdot, t + \Delta t) + \omega_L \Delta t (\tilde{f}_\alpha^{eq}(\cdot, t + \Delta t) - \tilde{f}_\alpha(\cdot, t + \Delta t)) \quad (4)$$

with equilibrium function

$$f_\alpha^{eq}(\rho, \mathbf{u}) = \rho t_\alpha \left[1 + \frac{3\mathbf{e}_\alpha \cdot \mathbf{u}}{c^2} + \frac{9(\mathbf{e}_\alpha \cdot \mathbf{u})^2}{2c^4} - \frac{3u^2}{2c^2} \right] \quad (5)$$

with $t_0 = 1/3$, $t_\alpha = 1/18$ for $\alpha = 1, \dots, 6$ and $t_\alpha = 1/36$ for $\alpha = 7, \dots, 18$. The variation in hydrodynamic pressure for the equilibrium function (5) is $\delta p = (\sum_\alpha f_\alpha^{eq} - \rho_0) c_s^2 = (\rho - \rho_0) c_s^2$. It can be shown by applying a Chapman-Enskog expansion procedure [10] that the sketched LBM converges to a solution of the weakly compressible Navier-Stokes equations

$$\partial_t \rho + \nabla \cdot (\rho \mathbf{u}) = 0, \quad (6)$$

$$\partial_t \mathbf{u} + \mathbf{u} \cdot \nabla \mathbf{u} = -\nabla p + \nu \nabla^2 \mathbf{u}. \quad (7)$$

Furthermore, it can be shown, cf. [9], that for this LBM the laminar kinematic viscosity ν_L , discrete laminar collision frequency ω_L , physical sound speed c_s , and time step Δt are connected by the relation

$$\omega_L = \frac{c_s^2}{\nu_L + \Delta t c_s^2 / 2} \quad (8)$$

It is mandatory to apply a turbulence model in high Reynolds number situations. In the context of LBM, it is common to adopt a large eddy simulation approach and assume that the partial density distribution functions used in the scheme represent the resolved scales. The influence of subgrid scale turbulence is considered by adding a turbulent viscosity ν_t to the physical laminar one. The effective viscosity $\nu^* = \nu_L + \nu_t$ is then utilized throughout the scheme. Like Hou et al. [10], we apply the Smagorinsky model to evaluate ν_t , for which $\nu_t = (C_{sm}\Delta x)^2 \bar{S}$ is used, with

$$\bar{S} = \sqrt{2 \sum_{i,j} \bar{S}_{ij} \bar{S}_{ij}}, \quad \bar{S}_{ij} = -\frac{1}{2\rho c_s \tau_L} \sum_{\alpha} \mathbf{e}_{\alpha i} \mathbf{e}_{\alpha j} (\bar{f}_{\alpha} - \bar{f}_{\alpha}^{eq}), \quad (9)$$

where \bar{f} and \bar{f}^{eq} are the filtered particle density distribution and the filtered equilibrium particle density distribution, respectively. The effective relaxation frequency, ω^* , is then obtained from

$$\omega^* = 2 / \left(\sqrt{\omega_L^{-2} + 18\sqrt{2}\rho^{-1}c_s^{-2}(C_{sm}\Delta x)^2\bar{S}} - \omega_L^{-1} \right) \quad (10)$$

and used in place of ω_L in the collision operation (4).

1.2 Dynamic Mesh Adaption

For local dynamic mesh adaption we have adopted the block-structured adaptive mesh refinement (SAMR) method after Berger & Collella [2]. In order to fit smoothly into our existing, fully parallelized finite volume SAMR software system AMROC [8], we have implemented the LBM cell-based, which makes the scheme also conservative in ρ and ρu_i . In the SAMR approach, finite volume cells are clustered with a special algorithm into non-overlapping rectangular grids. The grids have a suitable layer of halo cells for synchronization and applying inter-level and physical boundary conditions. Refinement levels are integrated recursively. The spatial mesh width Δx_l and the time step Δt_l are refined by the same factor r_l , where we assume $r_l \geq 2$ for $l > 0$ and $r_0 > 1$. Note that in an adaptive LBM the collision frequency ω_L is not a constant but needs to be adjusted according to Eq. (8) for the update on each level. In addition to this, the interface region requires a specialized treatment. Distinguishing between the transport and collision operators, T and C , cf. Eqs. (2) and (4), the crucial steps of our method are:

1. Use coarse grid distributions $f_{\alpha,in}^{c,n}$ that propagate into the fine grid, cf. Figure 2a, to construct initial fine grid halo values $f_{\alpha,in}^{f,n}$, cf. Figure 2b, by interpolation.
2. Transport $\tilde{f}_{\alpha}^{f,n} := T(f_{\alpha}^{f,n})$ on entire fine mesh. Collision $f_{\alpha}^{f,n+1/2} := C(\tilde{f}_{\alpha}^{f,n})$ is applied only in the interior cells (yellow in Figure 2b). Repeat $r_l - 1$ times.
3. Average outgoing distributions from fine grid halos (Figure 2c) to obtain $\tilde{f}_{\alpha,out}^{C,n}$
4. Reverse transport for averaged outgoing distributions, $\bar{f}_{\alpha,out}^{C,n} := T^{-1}(\tilde{f}_{\alpha,out}^{C,n})$, and overwrite those in the previous coarse grid time step, cf. Figure 2d.
5. Repeat LBM update on coarse grid cells next to coarse-fine boundary only.

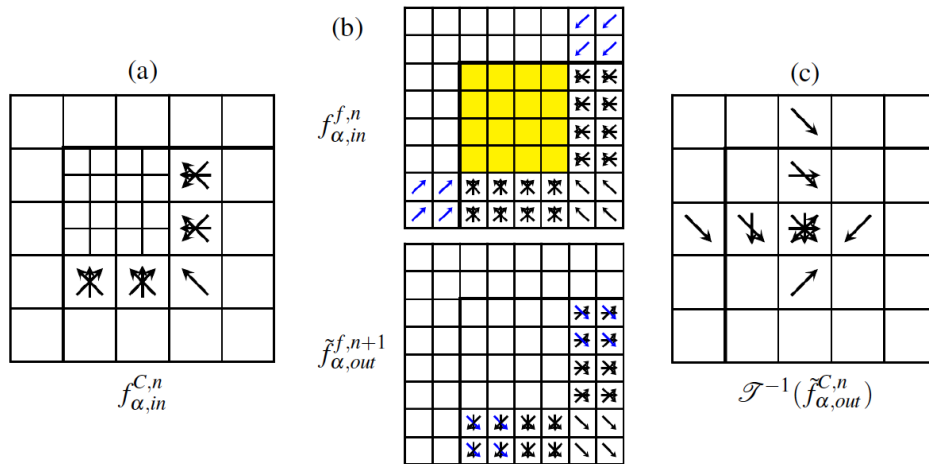


Figure 2. Visualization of distributions involved in necessary data exchange at a coarse-fine boundary. The thick black lines indicate a physical boundary. (a) Coarse distributions going into fine grid; (b) ingoing interpolated fine distributions in halos (top), outgoing distributions in halos after two fine-level transport steps (bottom); (c) averaged distributions replacing coarse values before update is repeated in cells next to boundary.

This algorithm is computationally equivalent to the method by Chen et al. [6] but tailored to the SAMR recursion that updates coarse grids in their entirety before fine grids are computed. Because of the nonlinearity of the collision operator C it becomes necessary under this paradigm to repeat the LBM update for those coarse grid cells that share a face or corner with a fine grid.

1.3 Embedded Structures

We represent non-Cartesian boundaries implicitly on the adaptive Cartesian grid by utilizing a scalar level set function φ that stores the distance to the boundary surface. The boundary surface is located exactly at $\varphi = 0$ and the boundary outer normal in every mesh point can be evaluated as $\mathbf{n} = -\nabla\varphi/|\nabla\varphi|$. We treat a fluid cell as an embedded ghost cell if its midpoint satisfies $\varphi < 0$.

In order to implement non-Cartesian boundary conditions with the LBM, we have chosen to pursue a 1st order accurate ghost fluid approach that was already available in AMROC [7]. In our technique, the density distributions in embedded ghost cells are adjusted to model the boundary conditions of a non-Cartesian reflective wall moving with velocity \mathbf{w} before applying the unaltered LBM. The last step involves interpolation and mirroring of ρ , \mathbf{u} across the boundary to obtain ρ' , \mathbf{u}' and modification of the macro velocity in the immersed boundary cells to $\mathbf{u}' = 2\mathbf{w} - \mathbf{u}^*$, cf. [8]. From the newly constructed macroscopic values the density distributions in the embedded ghost cells are simply set to $f_{\alpha}^{eq}(\rho', \mathbf{u}^*)$.

The dynamics of multi-body systems undergoing interaction with the fluid are modeled as sets of triangulated surface meshes configured in kinematic chains. The dynamics of these mechanisms are solved by a recursive Newton-Euler method at each time step [26]. Considering an arbitrary link with a coordinate frame located at point P that is not coincident with its associated body's center of mass, the force and torque applied by the preceding link are

$$\begin{pmatrix} \mathbf{F} \\ \boldsymbol{\tau}_P \end{pmatrix} = \begin{pmatrix} m\mathbf{1} & -m[\mathbf{c}]^{\times} \\ m[\mathbf{c}]^{\times}I_{cm} & -m[\mathbf{c}]^{\times}[\mathbf{c}]^{\times} \end{pmatrix} \begin{pmatrix} \mathbf{a}_P \\ \boldsymbol{\alpha} \end{pmatrix} + \begin{pmatrix} m[\mathbf{w}]^{\times}[\mathbf{w}]^{\times}\mathbf{c} \\ I_{cm} - m[\mathbf{c}]^{\times}[\mathbf{c}]^{\times}\mathbf{w} \end{pmatrix} \quad (11)$$

Here, we additionally define the total force and torque acting on a body, $\mathbf{F} = (\mathbf{F}_{FSI} + \mathbf{F}_{prescribed}) \cdot \mathbf{C}_{xyz}$ and $\boldsymbol{\tau} = (\boldsymbol{\tau}_{FSI} + \boldsymbol{\tau}_{prescribed}) \cdot \mathbf{C}_{\alpha\beta\gamma}$ respectively. Where \mathbf{C}_{xyz} and $\mathbf{C}_{\alpha\beta\gamma}$ are the translational and rotational constraints, respectively. \mathbf{F}_{FSI} and $\boldsymbol{\tau}_{FSI}$ are determined for each body by integrating the fluid pressure on the triangular facets of the respective body's surface mesh. Each surface mesh is associated with a kinetic link in a chain that begins with a base link in the global coordinate frame. Links are connected by joints that may be independently constrained in six degrees of freedom relative to the preceding link. The evolution of the triangular surface mesh as well as the velocity \mathbf{w} in each node is communicated to the LBM fluid solver in dedicated coupling time steps. The data exchange corresponds to the time step of an SAMR level but this does not have to be the finest refinement level available, cf. [7].

2 HINGED WING VERIFICATION CASE

A canonical problem of fluid-structure interaction and wake prediction proposed by Toomey & Eldredge [25] is selected as a validation test case for coupled aerodynamics simulation. This model, depicted in Figure 3, utilizes a system of two articulated rigid bodies connected by a torsion spring and damper. The kinematics of the centroid of the driven wing are prescribed, while the trailing body responds passively to the aerodynamic and inertial/elastic forces. The principle unknown in this rigid body dynamics problem is the hinge angle, θ . The parametric kinematic equations

$$X_1(t) = \frac{A_0}{2} \frac{G_t(ft)}{\max G_t}, \quad \alpha_1(t) = -\beta \frac{G_r(ft)}{\max G_r}, \quad (12)$$

$$C(t) = \frac{\tanh(8t-2) + \tanh(2)}{t + \tanh(2)}, \quad (13)$$

$$G_t(t) = \int_t \tanh(\sigma_t \cos(2\pi t')) dt', \quad (14)$$

$$G_r(t) = \int_t \tanh(\sigma_r \cos(2\pi t')) dt', \quad (15)$$

$$G_r(t) = \tanh(\sigma_r \cos(2\pi t + \Phi)) \quad (16)$$

describe the motion of the driven body. The parameters used in this work and [1] to specify the kinematics through the translational, $G_t(t)$, and rotational, $G_r(t)$, shape functions are presented in Table 1. A start-up conditioner, $C(t)$, is applied to the translational kinematics to avoid an impulsive start. The translational and rotational Reynolds numbers are based upon the peak translational, V , and rotational, $2\pi\beta\sigma_r f c \tanh(\sigma_r)$, velocities as

$$\text{Re}_t = Vc/\nu, \quad \text{Re}_r = 2\pi\beta\sigma_r f c^2 / (\tanh(\sigma_r)\nu) \quad (17)$$

The torsion spring and damper coefficients are $K^* = 6.9 \cdot 10^{-3} \text{kg m}^2/\text{s}^2$ and $R^* = 3.8 \cdot 10^{-4} \text{kg m}^2/\text{s}^2$, respectively. A no-slip boundary condition is applied at the ellipsoid surfaces and at the top and bottom (y -direction). The simulation domain is a box of extents $x: [-0.5, 0.5]$, $y: [-0.5, 0.5]$, $z: [-0.31, 0.31]m$. It is periodic in the x -direction and has slip walls at the z -boundaries to minimize corner effects similar to the configuration used by Aono et al. [1].

Table 1. Hinged Wing Kinematic Parameters.

A_0 (cm)	7.1	Φ	0, 45
c (cm)	5.1	Re_t	73, 370
d (cm)	0.25	Re_r	100, 500
β	$\pi/4$	ρ_b (kg/m^3)	5080
σ_t	0.628, 1.885, 3.770	f (Hz)	0.15
σ_r	0.628, 1.885, 3.770		

The errors in mean and peak forces and moments relative to the values predicted by the VVPM [25] are shown in Tables 4 and 5, respectively. The spatial and temporal resolution at the wing surface in Case 2.2 predicts peak hinge deflection, forces and moment accurately at moderate computational cost. These parameters were selected to simulate the seven kinematic cases investigated by Toomey & Eldredge [25]. Eddies shed by the moving wing in Case 2 are clearly depicted in the vorticity field at two times in Figure 4. Regions of mesh refinement and the domain decomposition displayed in Figure 5 plainly present the adaptive refinement and load balancing during runtime within AMROC. Hinge deflections for Case 2 are presented in Figure 6 and are in good agreement with the experimental results [25].

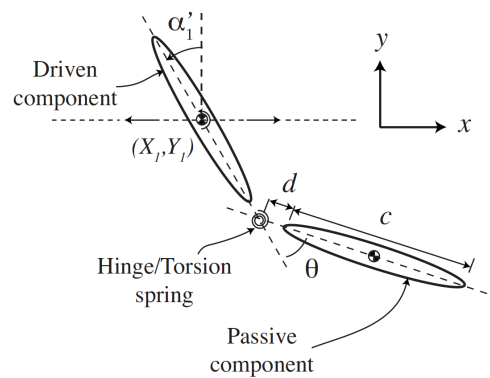


Figure 3. Model system of two rigid elliptical bodies connected by a hinge with torsion spring and damper.

Table 2. Hinged Wing Convergence Study Parameters.

Case	2.1	2.2	2.3	2.4
$ \nabla\vec{v} $	0.5	0.5	0.5	0.5
net refine	0.125	0.0625	0.0625	0.0625
finest $\Delta x/c$	2.45E-02	1.22E-02	6.12E-03	3.06E-03
finest $\Delta t/\tau_r$	3.53E-04	8.83E-05	4.42E-05	2.21E-05

Table 3. Hinged Wing Convergence Study Parameters.

Case	$Re_r = 100$			$Re_r = 500$		
	Mean	Peak	Wall [s]	Mean	Peak	Wall [s]
Ref.	-0.124°	17.167°	-	-0.116°	17.980°	-
2.1	-8.31%	-0.95%	625	-8.08%	-0.93%	656
2.2	-8.31%	-0.81%	2047	-8.01%	-0.79%	2118
2.3	-2.11%	-0.03%	7630	-2.08%	-0.03%	7974
2.4	-2.01%	-0.01%	43318	-2.00%	-0.01%	44834

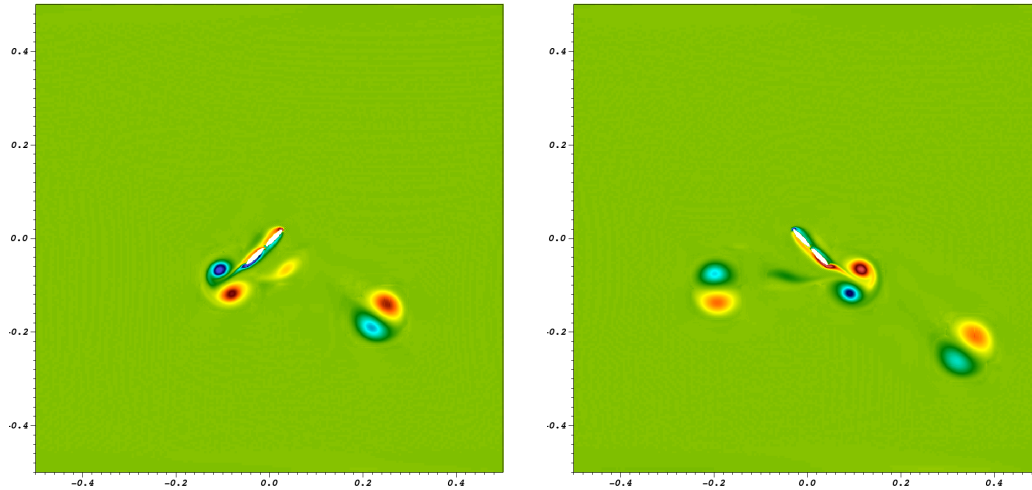


Figure 4. CASE 2.2 $\sigma_t = 1.85$, $\sigma_r = 1.885$, $\Phi=0$ $Re_r = 100$: vorticity at $t/\tau_r = 1.05$ (left), 1.58 (right).

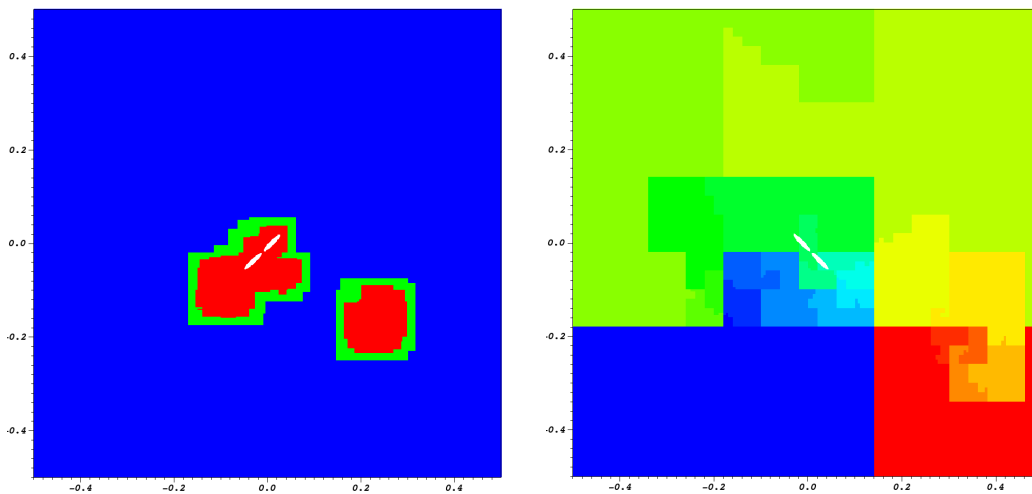


Figure 5. CASE 2.2 $\sigma_t = 1.85$, $\sigma_r = 1.885$ $\Phi=0$ $Re_r = 100$: 3 refinement levels at $t/\tau_r = 1.05$ (left), domain distributions to 24 processors at $t/\tau_r = 1.58$ (right).

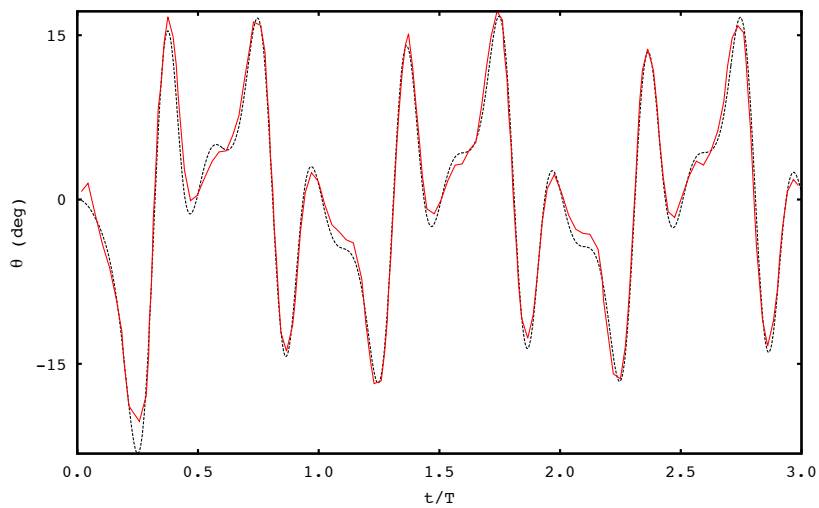


Figure 6. CASE 2 $\sigma_t = 1.85$, $\sigma_r = 1.885$, $\Phi=0$: Hinge deflection angle over time. Experimental results (-); Current (- -).

3 SINGLE TURBINE SIMULATION

Utilizing the developed LBM solver for moving geometries, we have carried out a simulation campaign to test the suitability of the overall approach to simulate the flow fields created by wind turbines. We have built a tailored flexible surface mesh model of a Vestas V27 turbine. The V27 has a rotor diameter of $D=27\text{m}$, a tower height of $\sim 35\text{m}$ and achieves its maximal energy output of 225kW at wind velocities from 14 to 25m/s . A prototypical ground topography is also included into the surface mesh model that represents the time-dependent geometry with $\sim 23,300$ facets per turbine. It is assumed that the inflow wind direction is always in direction of the turbine middle axis and the pitch blade angle is at 0 degrees.

In the first computation, Case 1, the wind velocity is $u_x=7\text{m/s}$ with a boundary layer profile of 5m height assumed near the ground and the turbine is operating at 15rpm . A simulation domain of extents $200\text{m}\times 100\text{m}\times 100\text{m}$ is used and discretized with a base grid of $400\times 200\times 200$ cells. Dynamic isotropic refinement with three additional levels refined by the factors 2 , 2 and 4 is applied. The two highest levels are reserved to refine the moving surface mesh of rotor and tower at a geometry resolution of $\Delta x=3.125\text{cm}$; level 1 is used to dynamically adapt to the wake region using an empiric error estimation criterion on $|u_x|$. Figure 7 shows snapshots of the moving structure colored by the surface pressure distribution. On the left of Figure 7 the stream wise velocity component on the turbine mid-plane depicts the recirculation region behind the tower and nacelle interacting with the blade vortices. On the right of Figure 7 the pressure field reveals near wake oscillations of ~ 100 dB SPL in agreement with the manufacturers specification of 97 dB SPL at hub height [28].

Figure 8 presents plots of instantaneous stream wise velocity at two upwind locations and four downwind locations along the central vertical plane at $t=8\text{s}$. The velocity deficit in the near wake is still pronounced 20m downwind. The impact of the tower is clearly shown below the bottom tip. The strong increases in velocity near the bottom tip height at 5m and 10m downwind indicate proximal tip vortices. The blade forces generate an average torque of ~ 185 kN-m in agreement with the prediction of 189 kN-m of torque from the rotor efficiency equation [4]. This computation was run on 80 cores of a cluster with Intel Xeon-Ivybridge CPUs and required $\sim 1,920\text{h}$ CPU in total, i.e., 24h wall clock time to simulate 10 seconds of wake production.

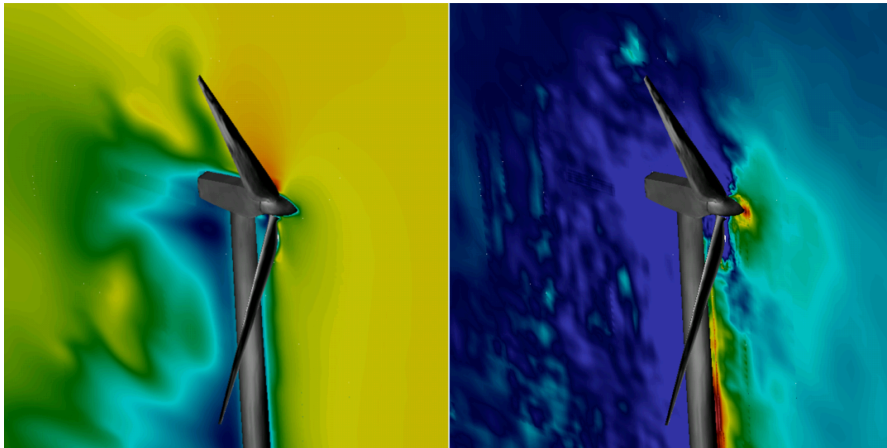


Figure 7. Case 1: Pressure colored turbine with stream wise velocity (left) and pressure (right) at $t=8\text{s}$.

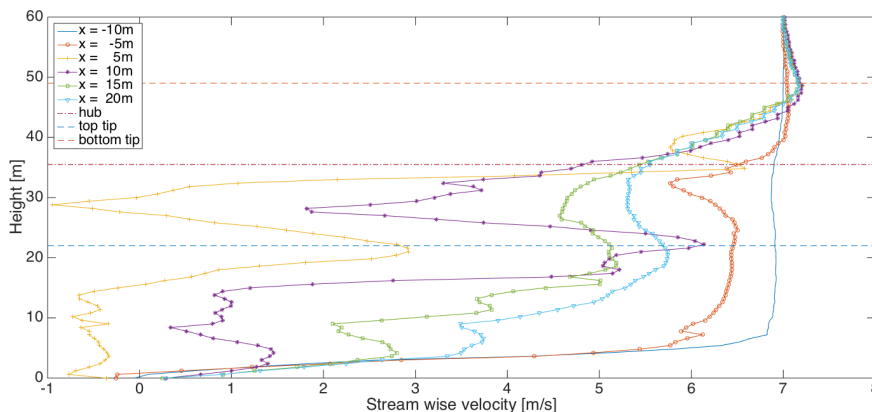


Figure 8. Case 1: Stream wise velocity profiles at $t=8\text{s}$.

In the second computation, Case 2, the wind velocity is $u_x=8\text{m/s}$ with a boundary layer profile of 5m height assumed near the ground and the turbine is operating at 33rpm . The domain, mesh, and refinement criterion are identical to those used in the first computation. Figure 9 presents plots of instantaneous stream wise velocity at the same six locations along the turbine mid-plane

as those used in Case 1 at $t=8s$. The increased oscillation of the streamwise velocity component is clear and can be attributed to the 220% increase in the rotational rate of the turbine between the cases and the corresponding increases in vortex strength and proximity in the near wake. The larger velocity deficit behind the turbine is also as expected for the higher tip speed ratio in Case 2.

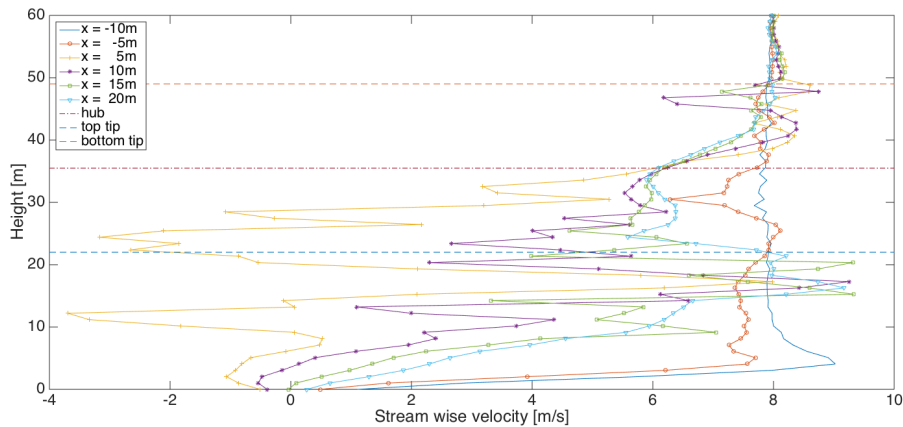


Figure 9. Case 2: Stream wise velocity profiles at $t=8s$.

The pressure and torque have been sampled every 0.034s on 18 radial sections along the blades. These values have been binned into 36 circumferential sectors and averaged over a 10 second interval beginning at $t=8s$. The reduction in streamwise pressure force due to blade-tower interaction is evident in Figure 10 (left) although the reduction in torque (right) is less distinct at these operational conditions. Comparable reductions in thrust and torques in the region adjacent to the tower have been obtained from simulations of the upwind configuration of the NREL 5MW reference turbine by Zhao et al. [31]. The mean pressure force torque produced corresponds to 81kW production, $C_e=0.44$, and $C_t=0.78$ which are all within 5% of the rated values at 8 m/s inflow [28]. In contrast an actuator disc model predicts 95 kW production, $C_e=0.53$, and $C_t=0.61$ for the 6.5m/s average streamwise velocity sampled across the rotor disc area [20][23].

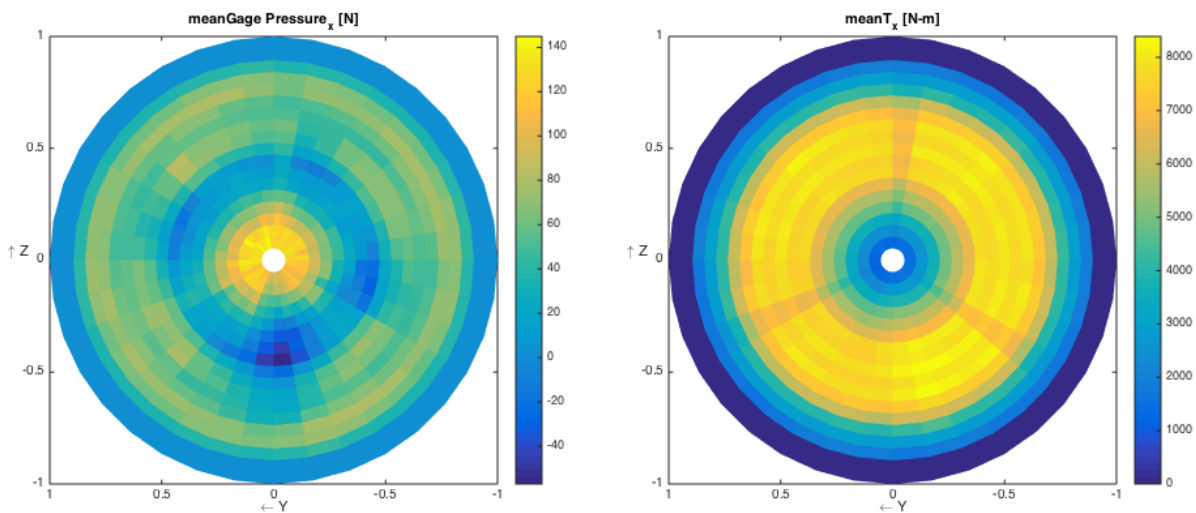


Figure 10. Case 2: Mean gage pressure force in streamwise direction on blades and mean torque over $t=[8,18]s$.

Sampling the flow field every 0.034s for 10s at 20 radial positions on 36 circumferential sectors of 6 circular regions, two upwind and four down wind of the turbine provide a richer view of the near wake. Figure 11 presents the mean gage pressure, streamwise velocity and their rms fluctuations 5m behind the tower center. The plots are scaled to the rotor diameter which is indicated by the red line. Samples are taken over 1.5 diameters to capture the near wake spreading. The low pressure low velocity recirculating region behind the tower and nacelle are clearly captured. The low streamwise velocity at the bottom of the sampling circle is due to the vortical structures emanating from the base of the tower and ground. The distribution of strong

fluctuations on this planar region 5m behind the turbine suggest the complexity of interactions between the rotor nacelle and tower.

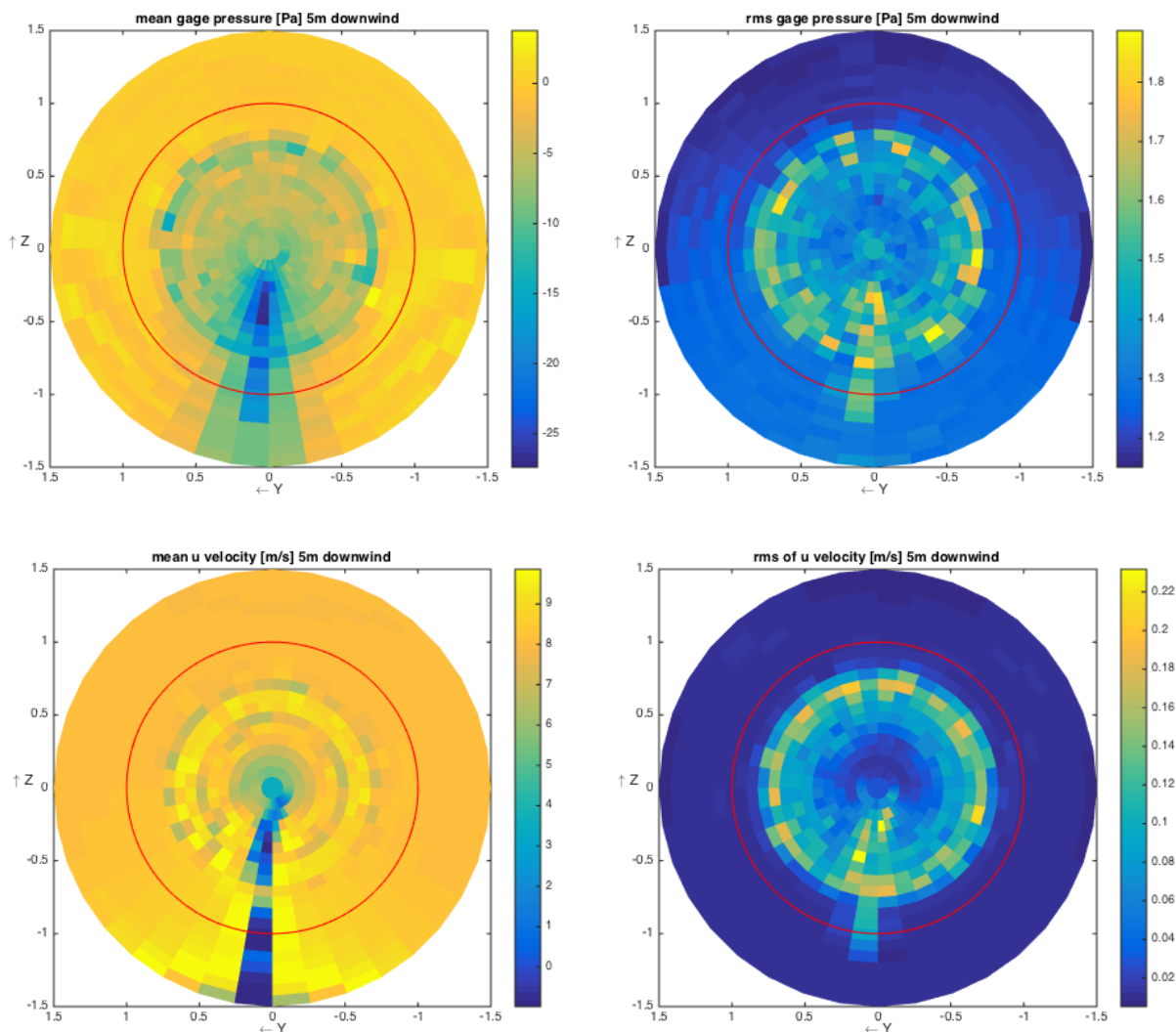


Figure 11. Case 2: Gage pressure, stream wise velocity and rms fluctuations 5m downwind of tower center over $t=[8,18]$ s.

The mean gage pressure, streamwise velocity and their rms fluctuations at 10m downwind are shown in Figure 12 for the same sampling and time interval. The peak pressure and velocity deficits and their rms fluctuations have evidently reduced and dispersed as they convected downwind from the previous sampling location. The deficits attributable to the nacelle in the inner region are recovering faster than those beyond the blade quarter span. The pronounced velocity fluctuations near $2/3$ rd of the blade span correspond to the high pressure and high torque regions of the rotor where most of the energy is extracted from the flow [14]. The tip vortices convect downwind smoothly and are more evident in the gage pressure plots than the velocity plots. While the tower's wake is still a clearly distinguishable feature in both the pressure and velocity fields as is the ground interaction.

As the flow reaches 15m downwind the nacelle deficit has recovered nearly 70% of the pressure and velocity losses observed at the 5m sampling station as can be seen by comparing Figures 11 and 13. The annular region of greatest fluctuations has migrated outward radially as the flow convected downwind. Within this annular region the greatest fluctuations are found just below the nacelle height where vortices from the rotor nacelle and tower confluence. The persistence of tower wake structures emanating from and interacting with the ground 15m downwind suggest that the tower plays a significant role in the turbine's wake beyond simply interrupting tip vortices as blades pass.

Figure 14 shows that while velocity recovery has continued to progress the deficit and fluctuations attributable to the tower are still significant in the mean flow 20m downwind. The mean gage pressure samples show that the wake continues to spread outward radially. The pressure fluctuations are largest at the confluence of wakes from the rotor nacelle and tower. It is also

notable that the pressure and velocity fluctuations are greater below hub height than above. This indicates that tower and ground vortex sheet interactions are playing a significant role in the progression of wake structures.

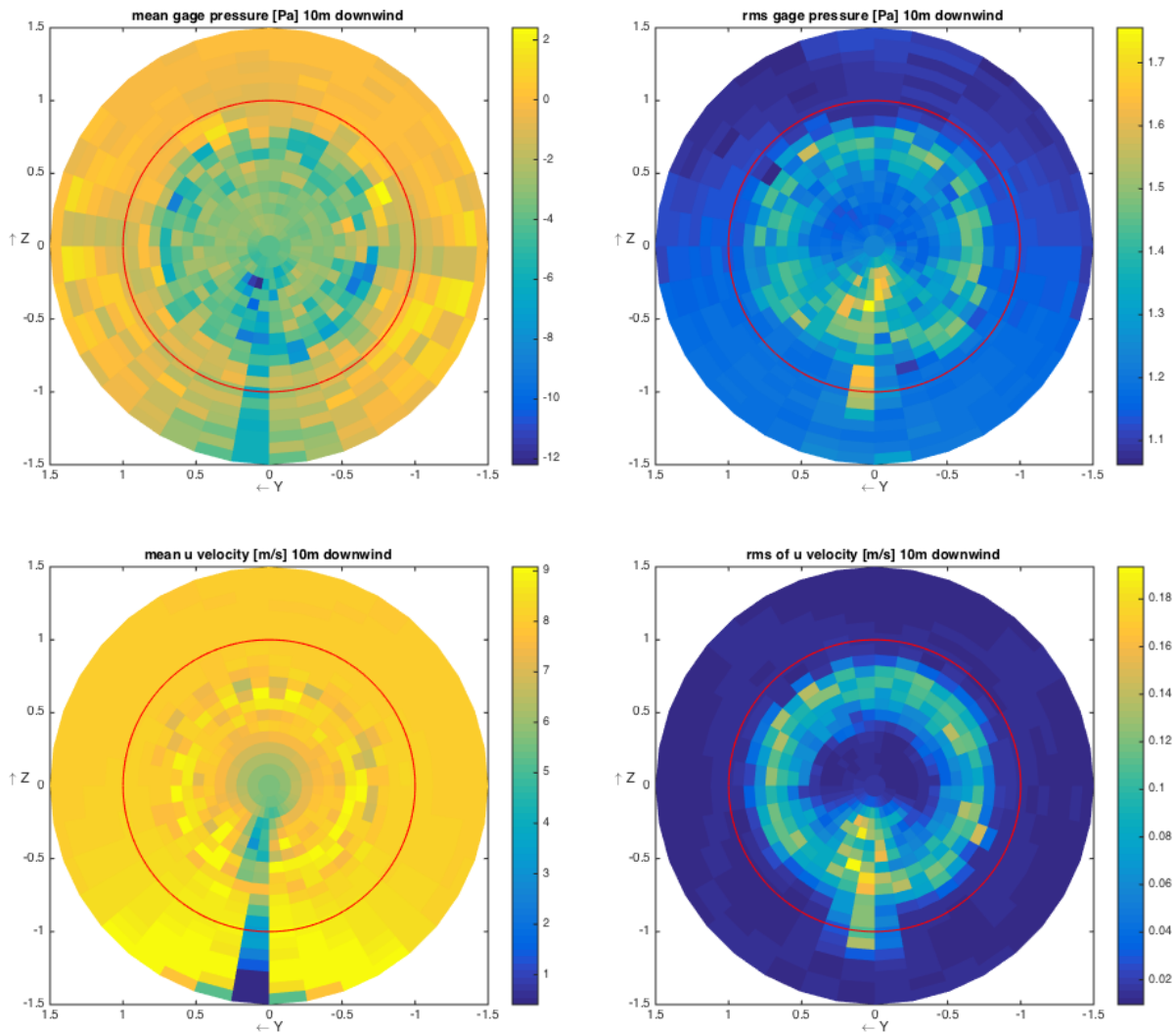


Figure 12. Case 2: Gage pressure, stream wise velocity and rms fluctuations 10m downwind of tower center over $t=[8,18]$ s.

The maximum values of gage pressure, streamwise velocity and their rms fluctuations are plotted in Figure 15. Normalizing the quantities by the maximum found at the 5m sampling plane shows that pressure recovery occurs most rapidly followed by streamwise fluctuations. Pressure fluctuations recover slowly and velocity deficit recovers only 11% over 15m. This indicates a significant and persistent momentum deficit in the wake and confirms the use of velocity as an empiric error estimation criterion to locate mesh refinement and thereby resolve wake structures.

The frequency content of the gage pressure sampled along the turbine's vertical center plane at three heights (hub, top tip, and bottom tip), and six windward positions at 29.4118Hz is shown in Figures 16-18. Examining the spectrums reveals the peak spectral density at all sampling positions occurs at 0.02163Hz well below the blade rotation frequency, n_0 of 1.65Hz. To account for this potent low frequency content we consider the tower as long cylinder of hydraulic diameter 0.85m in 8m/s inflow with viscosity of $1.61e-5 \text{ m}^2\text{s}^{-1}$ and obtain a Reynolds number of $4.224e5$, a Strouhal number of 0.2, and a shedding frequency of 0.0213Hz. The lowest frequency peak in the simulation is within 1.8% of the expected tower shedding frequency at all distances and heights sampled. This indicates the importance of including a realistic representation of a turbine's support structure when simulating a turbine's wake field.

Significant peak spectral densities are revealed at 2.595Hz, 4.325Hz, 7.785Hz, and 14.49Hz in the spectrum at hub height in Figure 16. The greatest of these occurs 15m downwind where the velocity deficit has flattened and begun to form a single peak. These three peaks are approximately n_0 , $2n_0$, and $4n_0$ apart indicating the influence of the blade rotation frequency on the wake at hub height. The spectrum at rotor top tip height shown in Figure 17 contains similar significant peaks at 2.595Hz, 4.325Hz,

and 14.71Hz. This spectrum correlates with blades and tip vortices dominating the wake field for all sampling positions at this height. The spectrum of the upwind positions shown in Figure 18 for the rotor bottom tip height contain significant peaks at approximately $in_0, i \in [1,9]$. These distinct peaks at rotor bottom tip height compared the lower amplitude and phase shifted peaks at hub and rotor top tip heights can be attributed to ground interaction through the lower portion of the power-law inflow profile. Down wind spectrums in Figure 18 also contain peaks at frequencies at 2.595Hz, 4.325Hz, 7.785Hz, and 8.867Hz similar in amplitude and spacing to the spectrum at hub and rotor top tip height indicating the tip vortices contribute to the turbulent energy within the wake region where tower wake and ground interaction are prevalent.

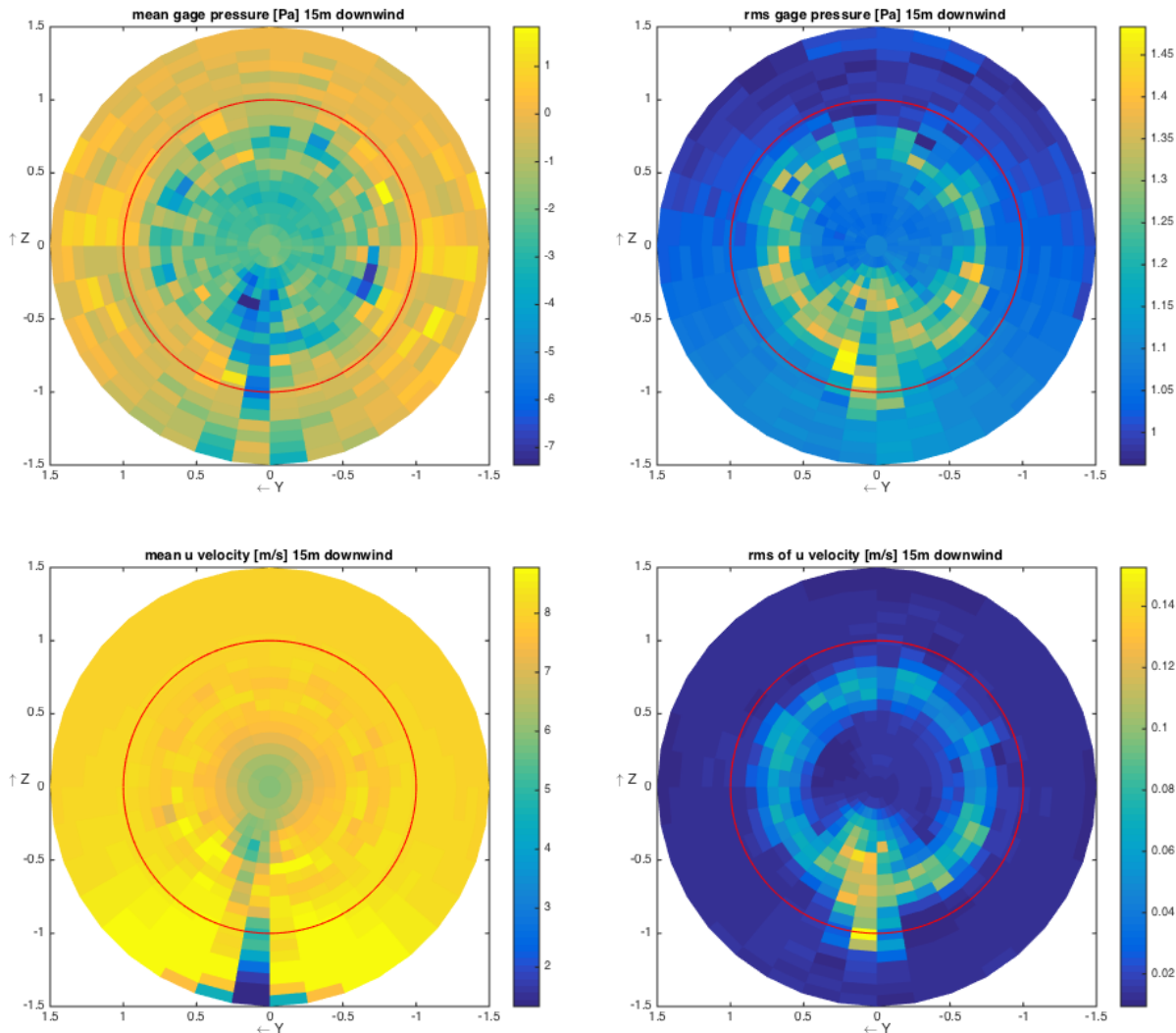


Figure 13. Case 2: Gage pressure, stream wise velocity and rms fluctuations 15m downwind of tower center over $t=[8,18]$ s.

Mo et al. carried out LES simulations of the wake behind a NREL Phase IV turbine and reported frequency content relating to the blade rotation frequency and similar decay in the near wake at hub height [15]. Porte-Agel et al. carried out LES simulations of the wake behind an actuator disc model of a three bladed turbine and reported a comparable trend in streamwise velocity fluctuations at hub height [18]. Examining the flow field at rotor tip heights in addition to hub height enables the influence of ground interaction and vertical entrainment on near wake turbulence to be investigated. Figures 19 and 20 present the power spectrum of the gage pressure difference between the rotor tips and hub. The prominent peaks in the spectra follow as expected from a comparison of Figures 16-18 but the extent of the deviation from hub height sampling particularly at low frequencies down stream is made clear in Figures 19 and 20. The maximum power spectral density of the deviation between the rotor top tip and hub height shown in Figure 19 occurs 20m downwind at 5.407Hz and -26.14 dB/Hz. The maximum difference between the rotor bottom tip and hub height also occurs 20m downwind at 4.109Hz and -15.49dB/Hz as displayed in Figure 20. Comparing these maximum differences reveals that tower and ground interactions reduce the deviation from values measured at hub height by 40.7% compared to the tip vortex dominated flow at the rotor top tip.

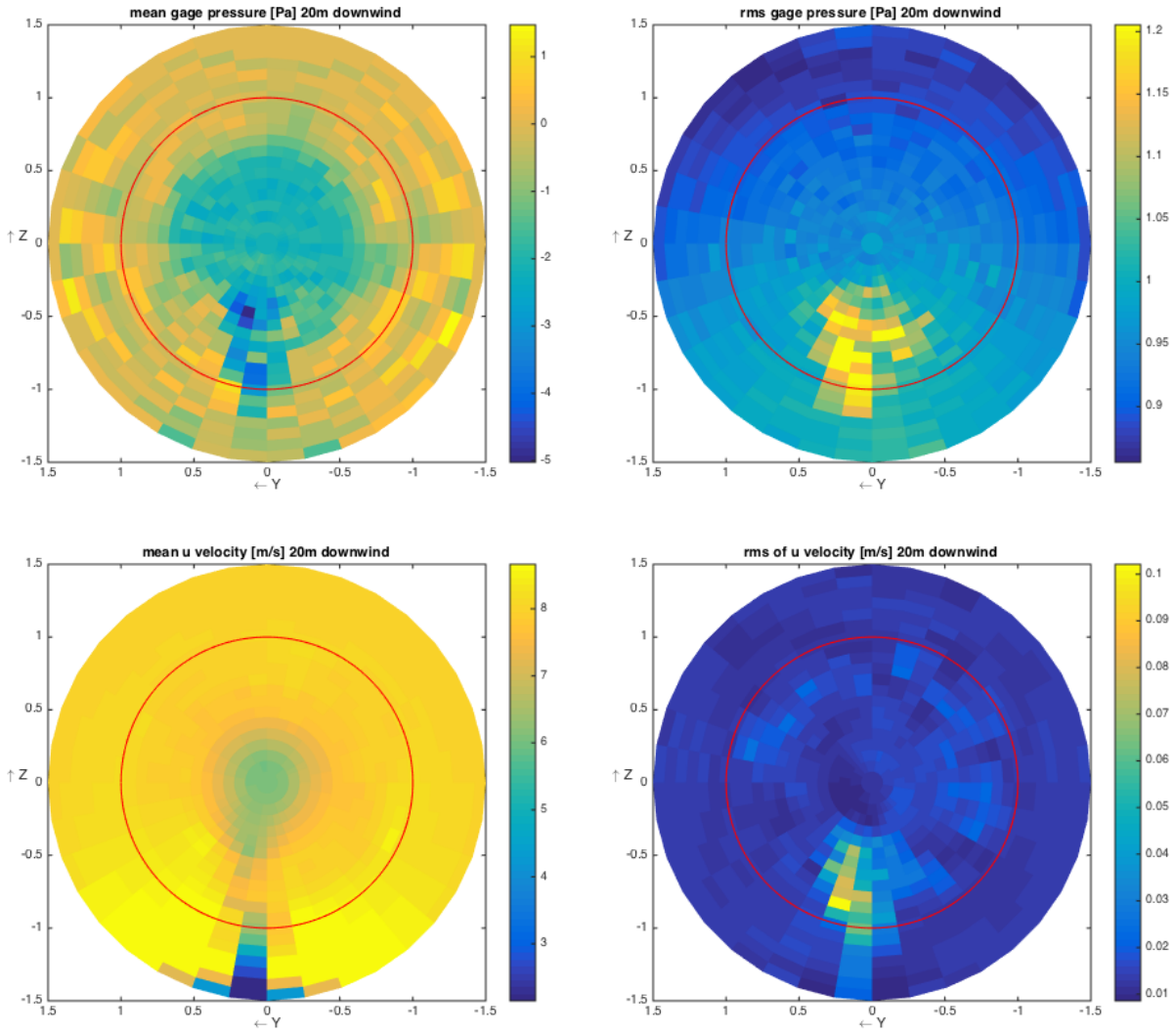


Figure 14. Case 2: Gage pressure, stream wise velocity and rms fluctuations 20m downwind of tower center over $t=[8,18]$ s.

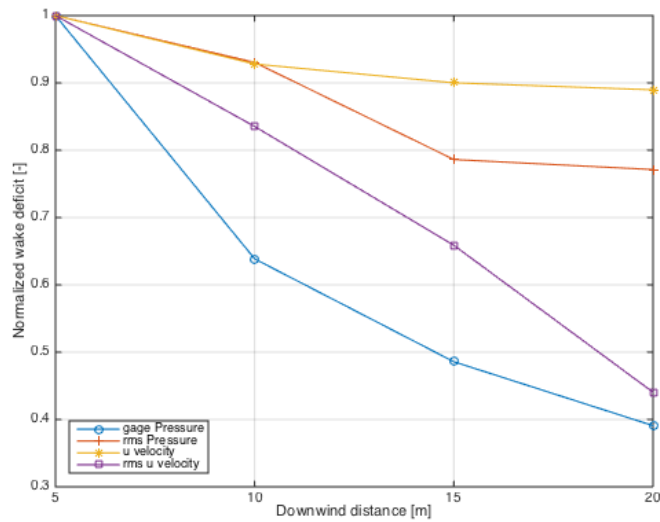


Figure 15. Case 2: Normalized maximum wake deficit gage pressures, streamwise velocities and their rms fluctuations from time average of $t=[8,18]$ s.

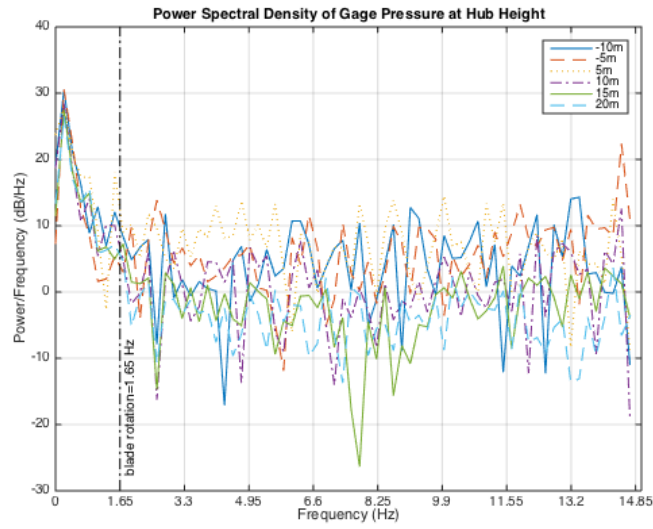


Figure 16. Case 2: Power spectrum of gage pressure at hub height for six locations sampled at 29.4118Hz.

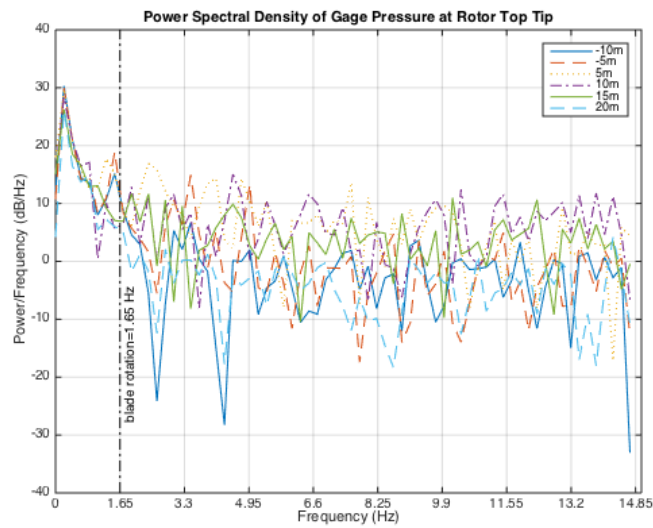


Figure 17. Case 2: Power spectrum of gage pressure at rotor top tip height for six locations sampled at 29.4118Hz.

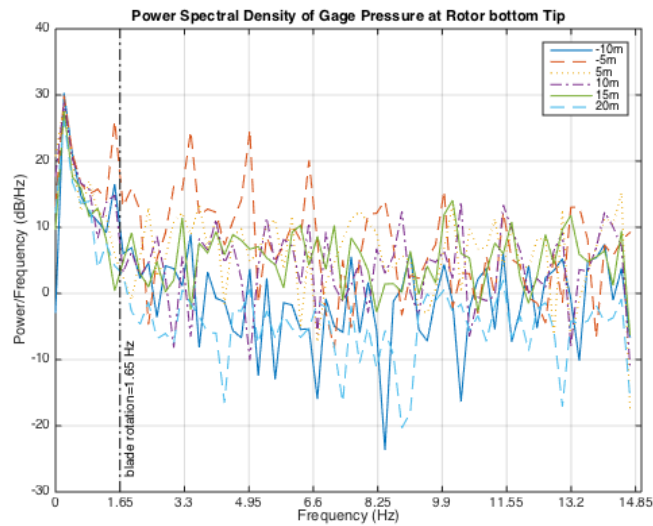


Figure 18. Case 2: Power spectrum of gage pressure at rotor bottom tip height for six locations sampled at 29.4118Hz.

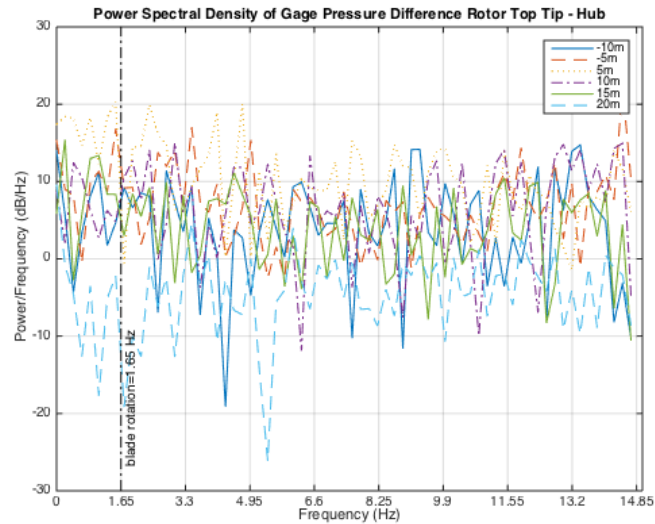


Figure 19. Case 2: Power spectrum of gage pressure difference between rotor top tip and hub heights for six locations sampled at 29.4118Hz.

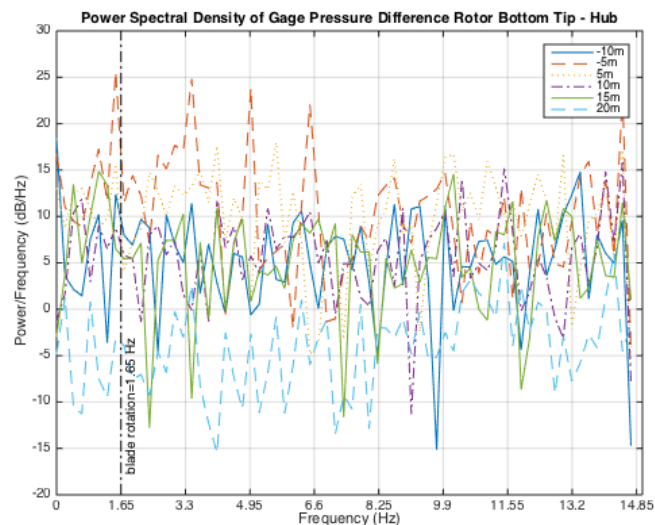


Figure 20. Case 2: Power spectrum of gage pressure difference between rotor top tip and hub heights for six locations sampled at 29.4118Hz.

4 TURBINE ARRAY SIMULATION

The array test setup considers three V27 turbines and corresponds to the U.S. Department of Energy's Scaled Wind Farm Technology (SWIFT) facility. Two turbines are positioned 3 rotor diameters apart in the wind direction; the third turbine is placed 5 rotor diameters downstream exactly in the rotor middle axis of the first one. This allows direct comparison of the wake field between two interacting turbines with an undisturbed one. The computational setup is similar to the previous simulations, where a domain of $488\text{m} \times 240\text{m} \times 100\text{m}$ is discretized with a base resolution of $448 \times 240 \times 100$ cells and again refined isotropically by the factors 2,2,4 (resolution near the rotors is $\Delta x = 6.25\text{cm}$). Figure 21 depicts the turbine and topography meshes along with sample points. In this simulation dynamic refinement of the wake field is permitted up to level 2, yielding again a resolution in the wake of $\Delta x = 25\text{cm}$.

Two configurations are compared: the case with $u_x = 7\text{m/s}$ inflow velocity and all turbines operating at 15rpm and a simulation with $u_x = 25\text{m/s}$ and 43rpm, which corresponds to the maximally allowed rotation rate under normal operations. 94,224 highest level iterations to a final time of $t_e = 40\text{s}$ are computed. Figure 22 depicts normalized streamwise velocity averaged over $t = [40, 50]\text{s}$ from sampling transects at hub height shown in Figure 21. The additional velocity deficit due to the downwind turbine is clearly visible on the left of Figure 22. The gradual recovery of the streamwise velocity behind the single turbine on the right of the array as shown in Figure 22 even as far as 11.11 rotor diameters downwind indicates the diminished flow energy available down wind of a single turbine well beyond the rule of thumb spacing of eight rotor diameters.

Figures 23 and 24 depict the wake fields for both cases after $t \approx 37s$ simulated time. The color-coding in both graphics uses the same scale and it is clearly shown that vorticity production is considerably increased in the second configuration. In both simulations, the radiuses of the main vortices increase slightly as they are transported downwind and vorticity is exceptionally well preserved overall. A strong influence of the tower on the wake field is apparent in both configurations. The difference between the wake fields behind the isolated turbine versus the two turbines aligned in the wind direction is striking.

Because of the higher wind velocity the number of vortex rotations between the upwind and downwind reduces in the second configuration from ~ 15 to ~ 12 . In both simulations, incident pressure and velocity on the downstream turbine are reduced (not shown). Its rotation apparently induces a less pronounced helical vortex than the upstream turbines. The used SAMR grids and total number of cells on each level for the second configuration at t_c are given in Table 4. Note that a corresponding uniform mesh would require 44×10^9 cells and take four times more time steps than level 2, which contains the majority of cells. A benchmark run on 288 cores on a cluster of Intel-Ivybridge CPUs required just 38.5h wall clock time (11,090h CPU) to advance this computation further from $t_c = 40$ to 50s, which gives evidence for the practical feasibility of carrying out these computations on compute clusters of moderate size.

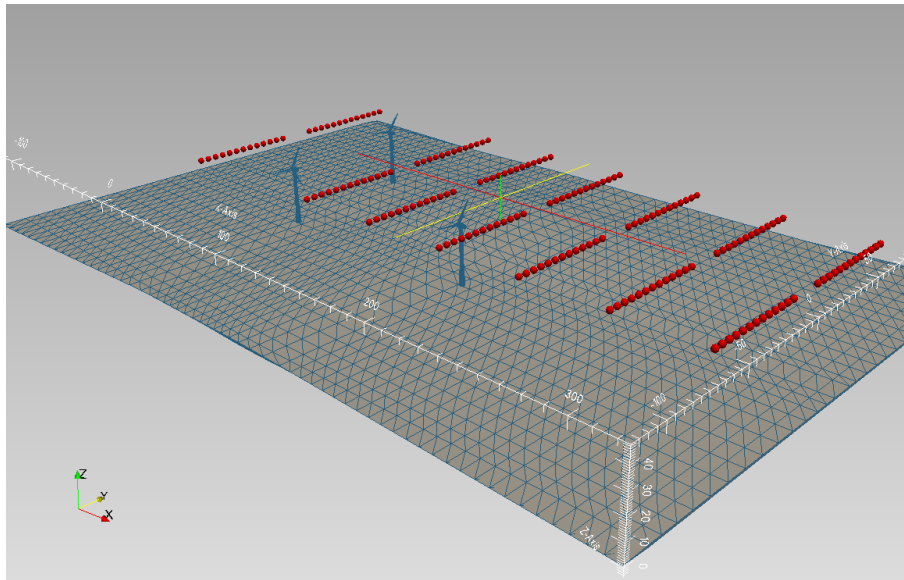


Figure 21. SWiFT Phase 1 simulation domain shown with turbine and topography meshes, and flow sample points.

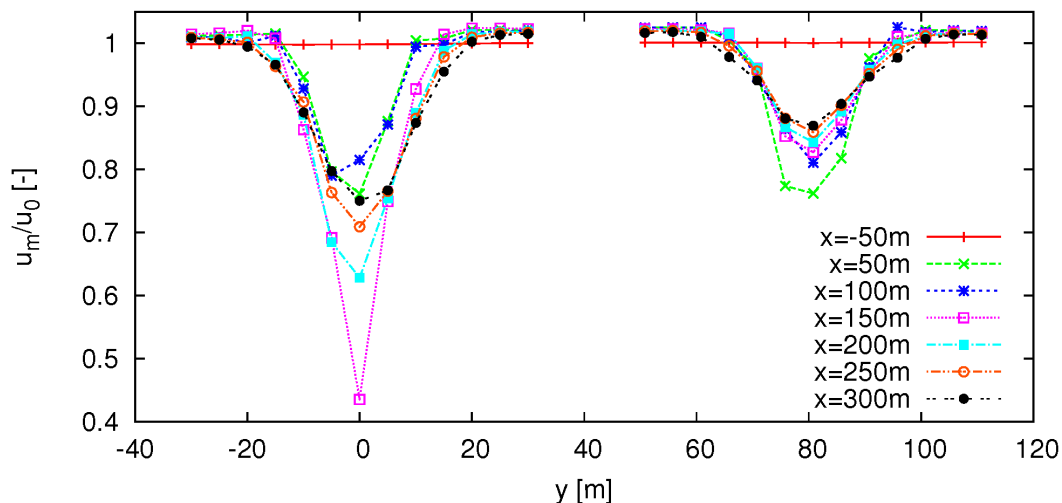


Figure 22. Normalized streamwise velocity sampled on hub height transects upwind and down wind of turbines in 25 m/s inflow operating at 43 rpm over $t=[40,50]s$.

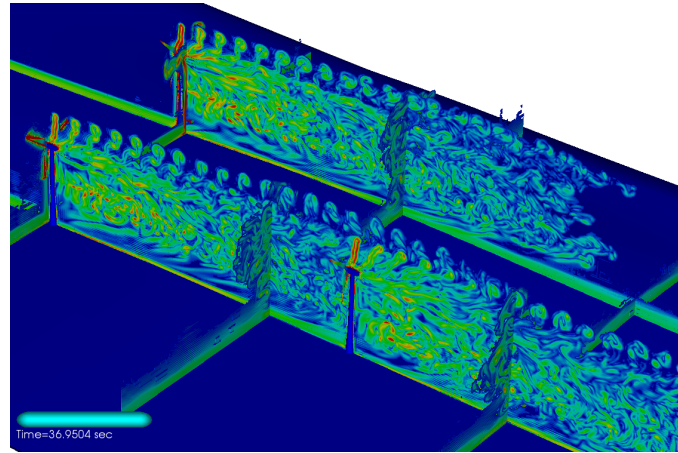


Figure 23. Color planes depict the magnitude of the vorticity vector for 7m/s mean inflow velocity at $t \approx 37s$.

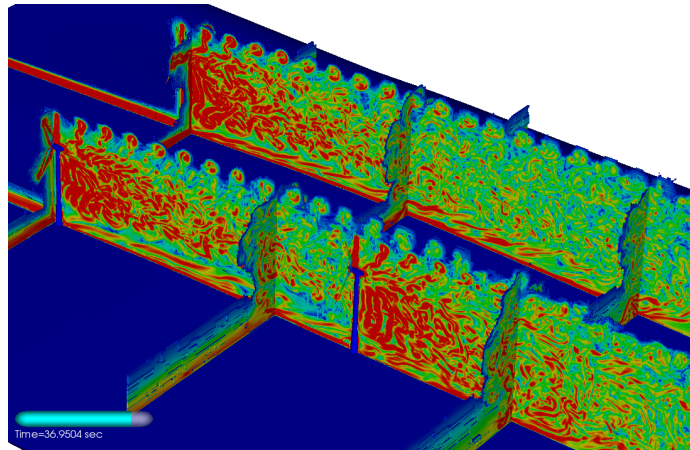


Figure 24. Color planes depict the magnitude of the vorticity vector for 25m/s mean inflow velocity at $t \approx 37s$.

Table 4. Grids and cells at t_c .

Level	Grids	Cells
0	3,234	10,752,000
1	11,9	21,020,256
2	66,974	102,918,568
3	896	5,116,992

5 CONCLUSIONS

The first prototype of a dynamically adaptive, three-dimensional lattice-Boltzmann method for simulating the wake fields behind realistic, rotating wind turbines has been developed. We have confirmed that our approach is able to simulate the propagation of wake fields created by the rotation of accurate Vestas V27 wind turbine rotor geometry, including the interaction with the nacelle, tower, and ground, with apparent good quality and comparably moderate computational costs. The results indicate that considering the nacelle, tower, and ground interactions are important to accurately simulate wake propagation.

Immediate future work will concentrate on validating the approach for available laboratory benchmarks, e.g., the Mexico wind tunnel experiments [21] and then to incorporate the dynamic elastic response of the blades into the turbine model.

6 OUTLOOK

Blade elasticity in the flapwise direction is considered first for the NREL 5MW reference turbine depicted in Figure 25. As a first step the flapwise deformation of the blades is modeled with Euler-Bernoulli beam equation. An instance of the beam solver receives the net aerodynamic load in the flapwise direction from 100 sections along a blade at each motion solver step and returns the deformed position. The computational setup is similar to the previous simulations, where a domain of $300m \times 240m \times 210m$ is discretized with a base resolution of $300 \times 240 \times 210$ cells and again refined isotropically by the factors 2,2,4 (resolution near the rotors is $\Delta x = 6.25cm$). The wind velocity is $u_x = 11.4m/s$ across the rotor with a $1/7^{th}$ power law profile with 20m/s maximum velocity above 200m. The turbine is operating at 16rpm, 0° pitch, and 0° yaw. The blade's aerodynamic and structural properties are specified by Jonkman et al. [11]. First results are shown in Figure 26 in comparison with recent work of Yu and Kwon where the aerodynamic loads and blade deformations are updated once a revolution [27]. On average the

tip deflection is within $0.005R$ (0.32m) which corresponds to a relative error of 6.6%. The difference in tip deflection and blade curvature between the present work and that of Yu and Kwon is thought to be attributable to our neglect, so far, of lead-lag and torsional blade deflections and the difference in coupling schemes of the two methods. Modeling the blades with a Timoshenko beam solver to consider full 3D deformation is an immediate next step.

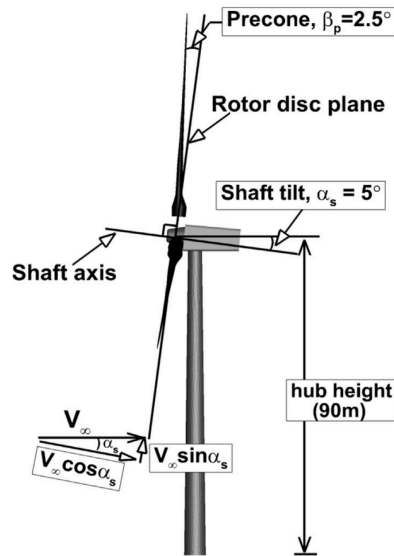


Figure 25. Sketch of NREL 5MW turbine highlighting geometric parameters pertinent to the blade flapwise direction [31].

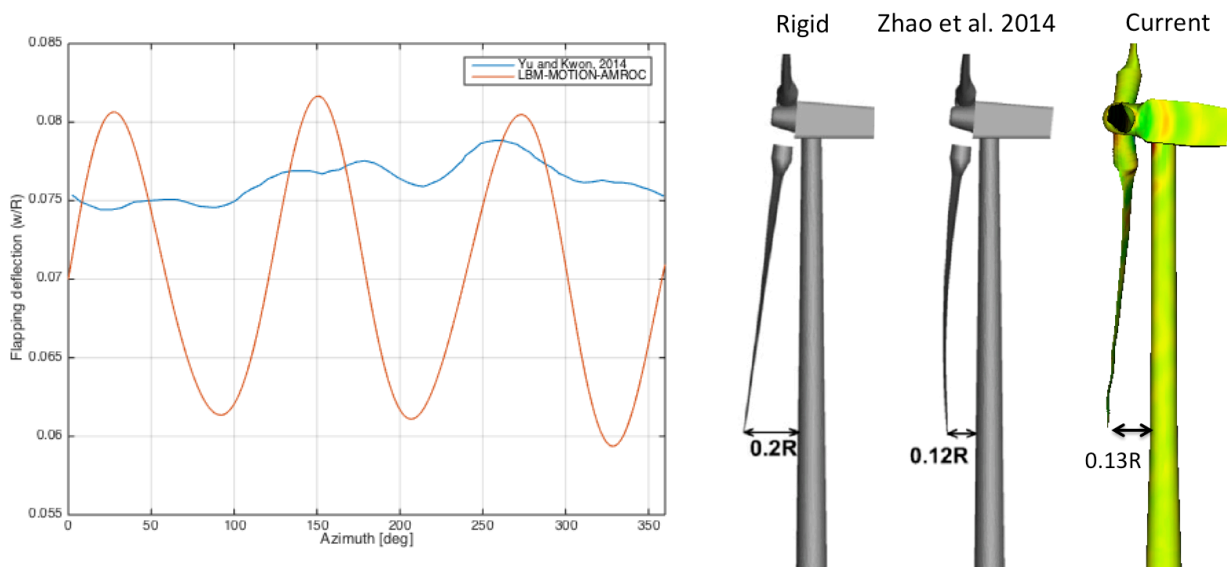


Figure 26. Flapwise tip deflection of a blade over one revolution (left). Comparison of closest tower passage of rigid blades, Zhao et al. simulations [31], and the current work (right).

ACKNOWLEDGMENTS

Stephen L. Wood was supported by the TN-SCORE Energy Scholar program funded by NSF EPS-1004083 during this work.

REFERENCES

- [1] H. Aono, A. Gupta, W. Shyy, The Lattice Boltzmann Method for Flapping Wing Aerodynamics, 40th Fluid Dynamics Conference and Exhibit, AIAA, 2010.
- [2] M. Berger and P. Colella, Local adaptive mesh refinement for shock hydrodynamics, *J. Comput. Phys.* 82, 64–84, 1988.
- [3] M. Carrión, R. Stejj, M. Woodgate, G.N. Barakos, X. Munduate, S. Gomez-Iradi, Aero elastic analysis of wind turbines using a tightly coupled CFD–CSD method, *J. Fluids and Structures*, 50, 392–415, 2014.
- [4] T. Burton, D. Sharpe, N. Jenkins, E. Bossanyi, *Wind Energy*, John Wiley and Sons Book Company, Chichester, England, 2001.
- [5] F. Castellani, A. Vignaroli, An application of the actuator disc model for wind turbine wakes calculations, *Applied Energy*, 101, 432–440, 2013.
- [6] H. Chen, O. Filippova, J. Hoch, K. Molvig, R. Shock, C. Teixeira, R. Zhang, Grid refinement in lattice Boltzmann methods based on volumetric formulation, *Physica A* 362, 158–167, 2006.
- [7] R. Deiterding, A parallel adaptive method for simulating shock-induced combustion with detailed chemical kinetics in complex domains, *Computers & Structures* 87, 769–783, 2009.

- [8] R. Deiterding Block-structured adaptive mesh refinement - theory, implementation and application, European Series in Applied and Industrial Mathematics: Proceedings 34, 97–150, 2011.
- [9] D. Hähnel, *Molekulare Gasdynamik*, Springer-Verlag Berlin Heidelberg, Germany, 2004.
- [10] S. Hou, J. Sterling, S. Chen, G.D. Doolen, A lattice Boltzmann subgrid model for high Reynolds number flows. In: A.T. Lawniczak, R. Kapral (eds.) *Pattern formation and lattice gas automata*, vol. 6, pp. 151–166. Fields Inst. Comm., 1996.
- [11] J. Jonkman, S. Butterfield, W. Musial, and G. Scott, Definition of a 5-MW Reference Wind Turbine for Offshore System Development, NREL/TP-500-38060, 2009.
- [12] H. Le, P. Moin, and J. Kim, Direct numerical simulation of turbulent flow over a backward-facing step. *Journal of Fluid Mechanics*, 330(1), 349-374, 1997.
- [13] S.P. Mauch, Efficient algorithms for solving static hamilton-jacobi equations, Ph.D. thesis, California Institute of Technology, 2003.
- [14] M. Magnusson, A.-S. Smedman, Air flow behind wind turbines, *J. Wind Eng. Ind. Aerodyn.* 80, 169-89, 1999.
- [15] J.O. Mo, A. Choudhury, M. Arjomandi, Y.H. Lee, Large eddy simulation of the wind turbine wake characteristics in the numerical wind tunnel model, *J. Wind Eng. Ind. Aerodyn.* 112, 11-24, 2013.
- [16] J.O. Mo, Y.H. Lee, Numerical simulation for prediction of aerodynamic noise characteristics on a HAWT of NREL phase VI. *Journal of Mechanical Science and Technology* 25, 1341–1349, 2011.
- [17] B. Montgomerie, The need for more measurements, Proc. 4th Int. Energy Agency (IEA) Aerodynamic Symp., Rome, Italy, 1990.
- [18] F. Porte-Agel, Y.T. Wu, H. Lu, R.J. Conzemius, Large-eddy simulation of atmospheric boundary layer flow through wind turbines and wind farms, *J. Wind Eng. Ind. Aerodyn.* 2011.
- [19] P.-E. Réthoré, N.N. Sørensen, A. Bechmann, Modelling issues with wind turbine wake and atmospheric turbulence, *Sci Making Torque, Wind*, 2010.
- [20] A. P. Schaffarczyk, *Introduction to Wind Turbine Aerodynamics*, Springer-Verlag Berlin Heidelberg, Germany, 2014.
- [21] J.G. Schepers, K. Boorsma, Final report of IEA task 29: Mexnext (phase 1) – Analysis of Mexico wind tunnel measurements. Tech. Rep. ECN-E-12-004, European research Centre of the Netherlands, 2012.
- [22] M. B. Schlaffner, Non-reflecting boundary conditions for the lattice Boltzmann method. PhD thesis, Technical University Munich, 2013.
- [23] D. A. Spera, Eds., *Wind Turbine Technology*, second edition, ASME, 2009.
- [24] M. A. Sprague, J. M. Jonkman, B. J. Jonkman, FAST Modular Wind Turbine CAE Tool: Nonmatching Spatial and Temporal Meshes, NREL/CP-2C00-60742, 2014.
- [25] J. D. Eldredge, J. Toomey, and A. Medina. On the roles of chord-wise flexibility in a flapping wing with hovering kinematics. *Journal of Fluid Mechanics*, 659:94–115, 9, 2010.
- [26] L. Tsai, *Robot Analysis: The Mechanics of Serial and Parallel Manipulators*, Wiley, 1999.
- [27] D. Yu, R. Mei, L.-S. Luo, W. Shyy, Viscous flow computations with the method of lattice Boltzmann equations, *Progress in Aerospace Sciences*, 39, 329-367, 2003.
- [28] Vestas, Vestas V27-225 kW, 50 Hz Wind turbine with tubular/lattice tower Item no.: 941129 Version 1.2.0.24, Vestas, 1994.
- [29] J. Whale, C.G. Anderson, R. Bareiss, S. Wagner, An experimental and numerical study of the vortex structure in the wake of a wind turbine, *J. Wind Eng. Ind. Aerodyn.* 84, 1-21, 2000.
- [30] S. Wagner, R. Bareiss, G. Guidati, *Wind Turbine Noise*, Springer-Verlag, Berlin Heidelberg, Germany, 1996.
- [31] Q. Zhao, C. Sheng, A. Afjeh, Computational Aerodynamic Analysis of Offshore Upwind and Downwind Turbines, *J. Aerodyn.*, 2014.